# Selective adsorption and transport of $CO_2$–$CH_4$ mixture under nano-confinement

Jian Wu [a], Luming Shen [a,*], Pengyu Huang [a,b], Yixiang Gan [a,c]

[a] School of Civil Engineering, The University of Sydney, NSW, 2006, Australia
[b] Hard Rock Mining, CSIRO Mineral Resources, QCAT, 1 Technology Court, Pullenvale, QLD, 4069, Australia
[c] Sydney Nano Institute, The University of Sydney, NSW, 2006, Australia

## ARTICLE INFO

## ABSTRACT

$CO_2$-enhanced gas recovery (EGR) is a promising technology to sequestrate $CO_2$ while enhancing $CH_4$ recovery simultaneously in shale reservoirs. During the process, the mixture of injected $CO_2$ and desorbed $CH_4$ of varied compositions flows within nanopores of shale. The nanoconfinement is known to affect single-component gas flow and transport significantly but has not yet been properly addressed for non-equimolar gas mixtures. Herein, we use molecular dynamics to systematically investigate the selective adsorption and transport of $CO_2$–$CH_4$ mixture in kerogen slit nanopores. Results show that the gas mixture velocity decreases logarithmically with increasing $CO_2$ molar ratio. The $CO_2$/$CH_4$ adsorption and transport selectivities are generally greater than one and have a strong negative correlation with the total pore gas pressure and pore size. The transport selectivity becomes rather important (i.e., much greater than one) when pore size is below 20 Å. Analyses indicate that surface adsorption and diffusion are primarily responsible for the selective transport, with bulk diffusion also playing a role. These findings provide nanoscale insights into the $CO_2$-EGR in shale's organic matrix and suggest that the selective transport of $CO_2$–$CH_4$ mixture should be considered in large-scale simulations under certain pore size and pressure conditions.

## 1. Introduction

The discovery and exploitation of shale gas are considered to have a positive impact on greenhouse gas (GHG) emissions in the global energy sector [1]. Over the past decade, $CO_2$ geologic sequestration has also emerged from a concept to a commercially feasible component of the clean energy transition to mitigate global warming [2,3]. Although saline aquifers can be popular options for the storage sites, depleted gas reservoirs such as shale may be more attractive for $CO_2$ storage as their pore pressure is below what existed before depletion, thus less likely to trigger earthquakes [4]. Moreover, shale gas production and $CO_2$ storage nowadays often come together, known as $CO_2$-EGR since shale gas production rate declines hyperbolically with time [5] and $CO_2$ injection can potentially enhance the limited transport of adsorbed gas from the matrix. The $CO_2$ storage potential of depleted unconventional shale reservoirs with enhanced $CH_4$ recovery has been confirmed by the first successful "huff-and-puff" $CO_2$ injection test conducted in Morgan County, Tennessee (US) where the daily gas production was over eight times the pre-injection average in the first month of flowback [6].

One of the most attractive aspects of $CO_2$ injection in shale reservoirs is the preferential adsorption of $CO_2$ over $CH_4$ in the organic matrix, which fundamentally differs from the storage mechanisms in saline aquifers [7]. The competitive adsorption between $CO_2$ and $CH_4$ has been studied extensively by laboratory experiments [8–11] and numerical simulations [12–18]. For example, Liu et al. [8] confirmed that $CO_2$ injection could induce dynamic desorption of adsorbed $CH_4$ by additionally ~25% in a sample of black shale core after performing the low-field Nuclear Magnetic Resonance (NMR) measurements. The results of Liu et al. [9] showed that increasing the $CO_2$/$CH_4$ partial pressure ratio in shale increased the adsorption capacity of $CO_2$ but decreased that of $CH_4$ logarithmically, and the competitive $CO_2$/$CH_4$ adsorption ratio (CAR) decreased logarithmically with the increasing total gas pressure as well. With the combination of gas chromatograph and conventional sorption experimental setup, binary mixture gas adsorption measurements were conducted in shale samples with varied $CO_2$/$CH_4$ molar ratios, where the preferential adsorption of $CO_2$ over $CH_4$ was widely recognized and the selectivity of $CO_2$ was found to change with pressure [19].

Molecular dynamics (MD) simulation is a valuable tool to reveal the underlying mechanisms of competitive sorption without the difficulty of separating free and adsorbed gases as in the laboratory experiments [8]. Using simplified organic and inorganic pore structures, Sun et al. [12] performed MD simulations in graphene-montmorillonite (MMT) slit pores with both homogeneous and heterogeneous surfaces and argued that the partial pressures of $CO_2$ and $CH_4$ played the decisive role in competitive gas adsorption at a fixed temperature and pore size. Interestingly, they found that gas adsorption on MMT surfaces was not sensitive to the partial pressure of the gas component. Kerogen is the primary hydrocarbon source of shale gas holding approximately one half of the adsorbed gas [20]. Ho et al. [13] performed grand canonical Monte Carlo-molecular dynamics (GCMC-MD) simulations for equimolar $CO_2$–$CH_4$ mixtures under various pressures and found that the adsorption selectivity of $CO_2$ over $CH_4$ was 3–6 within the over-mature kerogen nanoporous structure. Kerogen's organic type, maturity and moisture content can affect the competitive adsorption of $CO_2$-$CH_4$ mixtures. For example, Huang et al. [14] reported that the $CO_2$/$CH_4$ selectivity followed the order of kerogen type I < II < III in consistent with porosity values and changed nonmonotonically with moisture content. Sui et al. [15] found that the $CO_2$/$CH_4$ selectivity decreased with kerogen maturity as the N-, S-, and O-containing groups in kerogen had a greater impact on $CO_2$ adsorption than $CH_4$. Wang et al. [16] studied $CO_2$-$CH_4$ competitive adsorption in a kerogen slit pore under different geological pressure and temperature conditions, and inferred that the most proper injection depth for $CO_2$-EGR projects was 1.5–2.5 km below the surface. In theory, the greater isosteric heat of $CO_2$ than $CH_4$ adsorbed on kerogen surfaces justified the stronger adsorption capacity of $CO_2$ in kerogen slit nanopores [21]. More specifically, Ho and Wang [22] measured the interaction energies of $CO_2$ with kerogen II-D, pyrophyllite, gibbsite, and MMT as −6.2, −2.9, −5, and −5 kcal/mol, respectively, higher than (more negative) that of $CH_4$ with all these surfaces. They also reported that the interaction of $CO_2$ with the over-mature kerogen was stronger than that with other inorganic mineral surfaces.

Pores with size smaller than 50 nm constitute the majority of shale's porosity [23,24]. The nano-confinement leads to a unique gas flow and transport behavior distinct from the continuum scale, such as slip flow, Knudsen diffusion and surface diffusion [25–30]. In the context of gas mixtures, several studies have shown the selective transport and separation of gas components through nanopores [31–36]. Liu et al. [31] calculated the self-diffusion coefficients of $CO_2$ and $CH_4$ in both single-component and mixture gases, suggesting that the $CH_4$ and $CO_2$ self-diffusion coefficients could increase and decrease with the increase of $CO_2$ composition, respectively. However, the self-diffusion coefficients may not be appropriate for describing gas transport under a concentration gradient. Kazemi and Takbiri-Borujeni [32] simulated $CO_2$–$CH_4$ mixture diffusion in a graphene slit pore and concluded that the overall $CO_2$/$CH_4$ selectivity was negatively correlated to the total gas pressure. Specifically, the Fick's diffusion coefficient of each gas component increased with its partial pressure. They also found that the off-diagonal diffusion (by the chemical potential gradient of the partner gas component) had the same magnitude as the diagonal terms (by its own chemical potential gradient), and thus should not be ignored. Firouzi and Wilcox [33] examined the flow behavior of pure $CO_2$, $CH_4$, and their mixture in a single carbon slit pore under an external driving force and suggested that the gas velocity profiles would not always match each other for the 1:1 $CO_2$–$CH_4$ mixture as the transport of $CO_2$ was impacted more significantly by the pore walls compared with $CH_4$. Even though the kinetic diameter of $CO_2$ is less than that of $CH_4$, the greater impact mainly results from the higher affinity of $CO_2$ to the pore walls. For instance, the interaction energies of $CO_2$ and $CH_4$ molecules with a kerogen surface are −6.2 kcal/mol and −4.2 kcal/mol, respectively [22]. Based on the dual control volume-grand canonical molecular dynamics (DCV-GCMD), Wu and Firoozabadi [34] developed a new technique to simulate the transport and separation of the $CH_4$/He and

$CO_2$/$CH_4$ mixtures in slit pores by controlling the pressure of the permeate side through random deletion of molecules. They found that the gas mixture separation factor (i.e., selectivity) decreased as pore size increased from 0.8 to 2 nm, and then approached unity. Similarly, Ho et al. [35] observed a critical pore size (~1.8 nm) below which the selective transport of equimolar $C_2H_6$–$CH_4$ mixture could occur and argued that surface adsorption and diffusion were responsible for the selective transport. In addition, they suggested further work should be conducted with varied gas compositions other than 1:1 in clay and kerogen-based pores.

The existing literature greatly focuses on the competitive adsorption of binary $CO_2$–$CH_4$ gases at the nanoscale, which are mostly found in the operation of $CO_2$-EGR. There is a lack of studies on the multicomponent gas transport, and such investigations are limited to equimolar binary mixtures through the simplified inorganic/organic nano-pore structures. In this paper, we aim to systemically investigate the selective adsorption and transport of $CO_2$–$CH_4$ mixtures in shale's organic kerogen nanopores, subject to the influence of pore pressure (~2–30 MPa), gas composition (~10%–80% of $CO_2$) and pore size (10–60 Å). Firstly, we perform GCMC-MD simulations to build the initial gas saturation inside a slit pore confined between two over-mature kerogen slabs. Non-equilibrium molecular dynamics (NEMD) is then employed to simulate the pressure-driven gas flow and transport. Gas mixture velocity is studied as a function of gas composition under varied pore sizes, while $CO_2$/$CH_4$ adsorption and transport selectivities are analyzed as a function of pressure and pore size. The results can provide new insights into the gas production rate at different geological depths (i.e., pressure) as well as different stages (i.e., gas composition) of $CO_2$-EGR. Based on the adsorption and transport selectivities of $CO_2$/$CH_4$ mixtures, the gas compositions in shale reservoirs may be predicted from the produced gas compositions in real-time. The knowledge discussed here can also be potentially implemented into continuum scale simulations by upscaling.

## 2. Computational methods

As the main organic matter in shale, the type II-D kerogen units [37] are used to build the slit pore model in this study, which is an over-mature type from the Duvernay series and represents unconventional gas reserves such as the Barnett shale. Initially, 27 kerogen units are emplaced into an empty simulation box of 100 Å × 100 Å × 100 Å and relaxed by annealing in a few cycles. A wall of dummy particles is then added to the middle of the produced kerogen matrix, and the whole structure is relaxed again for separation (i.e., create two individual pieces of kerogen matrix). By adjusting the separation distance between two pieces of kerogen matrix in the z-dimension accordingly, different slit pore sizes can be created. As shown in Fig. 1, the kerogen slit pore model of size 10 Å is contained in a simulation box with a size of 45.24 Å × 45.61 Å × 55.31 Å. At the nanoscale, the amorphous kerogen walls are considered rough surfaces and have heterogeneous interaction forces with gas molecules. Therefore, the constructed slit pores are not perfectly straight. Our previous study on the single-component gas flow has shown that sorption-induced swelling can greatly affect the absolute gas adsorption and mass flux through the kerogen slit pore [38]. Therefore, the kerogen slit model is considered fully flexible in the present study and all kerogen matrix deformations are coupled into the results discussed herein. The kerogen, $CO_2$ and $CH_4$ molecules are described by the General Amber [39,40], TraPPE [41,42] and TraPPE-UA [43] force fields, respectively. The $CO_2$ molecule is rigidified with the C = O bond length fixed at 1.16 Å and the O = C = O angle at 180°. The non-bonded potential is calculated by the 12-6 Lennard-Jones potential with electrostatic force. Pair coefficients between different atom types are calculated by the Lorentz-Berthelot mixing rule. The cut-off is set at 14 Å and the long-range Coulombic term is calculated in the K-space by the particle-particle particle-mesh solver (PPPM) [44]. More simulation details, including the kerogen model and slit pore construction processes, can be found in our previous work [38,40,45].
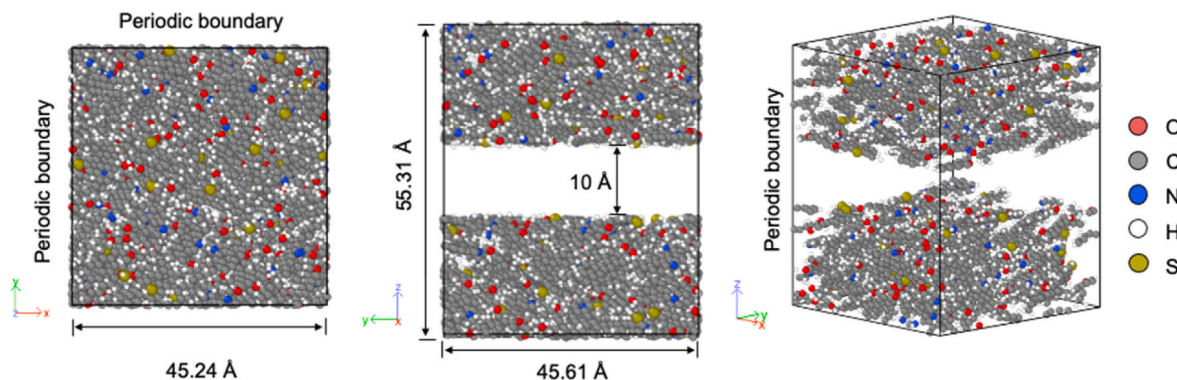
**Fig. 1.** Schematic of the kerogen slit pore model with boundary conditions.

Hybrid GCMC-MD simulations are performed to achieve the initial state of gas saturation while allowing the kerogen matrix to deform sufficiently in the meantime. The GCMC input chemical potentials for various $CO_2$–$CH_4$ compositions and total gas pressures are calculated from the Peng-Robinson equation of state [46] and have been testified in another set of GCMC-MD simulations with an empty simulation box in the absence of kerogen (see Table S1 and Fig. S1 in the supplementary materials). GCMC exchanges of gas molecules are conducted 50 times for $CO_2$ and 50 times for $CH_4$, respectively, after every 100 MD steps. The simulation is ceased when the numbers of $CO_2$ and $CH_4$ molecules converge after a typical period of 4 ns of MD relaxation. The NEMD simulation is subsequently conducted to generate pressure-driven flow by applying a force of 0.001 kcal/(mol•Å) on each gas particle (i.e., C, O and united $CH_4$ atoms) in the x-direction within the slit. The pressure drop along the slit pore length is calculated as

$$\Delta p = \frac{n_a F_a + n_b F_b + \dots}{A} \tag{1}$$

where, $n_a$ and $n_b$ are the numbers of particles $a$ and $b$, $F_a$ and $F_b$ are the forces applied on particles $a$ and $b$, and $A$ is the pore cross-section area. It has been shown that the pressure drop only depends on the total force imposed on the gas particles and the same velocity profile can always be obtained no matter how the constant total force is distributed among them [47]. Given sufficient running time of ~15 ns, the gas molecules can eventually reach a steady flowing state. The data between simulation time of 15 and 30 ns (and beyond) are selected to produce the velocity and density profiles of both $CO_2$ and $CH_4$ through spatial binning every 0.5 Å across the z-direction with a sampling frequency of 10 fs. Although only one kerogen type is used in this study, the reported data points are averaged values from over 1500,000 statistical samples, which represent 1500,000 different configurations of kerogen structures under a designed gas pressure and composition with the kerogen flexibility.

All the simulations are performed using LAMMPS [48] with a time-step of 1 fs under the NVT ensemble (constant atom number, volume, and temperature) at 300 K. Periodic boundary conditions are applied in the x-, y- and z-directions. OVITO [49] is used for the visualization of kerogen matrix and gas molecules. The $CO_2$ and $CH_4$ partial pressures and bulk molar compositions of the 60 Å and 40 Å slit pores are measured in a prescribed pore central region of height 10 Å, where the interaction from the kerogen surfaces is minimized. However, the bulk region is no longer identifiable when the pore size becomes smaller than 20 Å and the gas pressure cannot be directly measured within the pore. As an approximation, the average pressure from the bulk gas (without kerogen in the box) and large pore (60 Å and 40 Å) simulations that have the same inputted chemical potentials are used (Table S1).

## 3. Results and discussion

### 3.1. Density profiles

The $CO_2$–$CH_4$ mixture manifests different adsorption behaviors with respect to pore pressure, gas composition and pore size. A wide range of pore pressure is used here for a systematic investigation of the selectivity dependence on pressure, which may occur at different geological depths and reservoir depletion/$CO_2$ injection conditions. Fig. 2 provides an overview of the equimolar mixture adsorption in the kerogen slit pores of different sizes. It can be seen that in the 60 Å slit pore, a greater amount of $CO_2$ and $CH_4$ molecules distribute near the kerogen surfaces than in the pore center, while the difference gradually disappears as the pressure increases. In contrast, the entire 10 Å slit pore seems to be filled with gas molecules even at low pressure.

As shown in Fig. 3a, under the total gas pressure of ~3.0 MPa, both $CO_2$ and $CH_4$ form adsorption peaks close to the upper and lower kerogen surfaces in the 60 Å slit pore, and rise with the increase of the individual gas molar ratio in the bulk mixture. Compared with $CH_4$, $CO_2$ has a much higher adsorption peak due to its stronger interaction force with the kerogen surface [22]. The $CO_2$ peak is 13 times that of $CH_4$ under the $CO_2$:$CH_4$ bulk molar ratio of ~3:1 and three times under ~1:1. The results suggest that $CO_2$ can displace the $CH_4$ adsorbed at the kerogen surfaces even at low pressure and accumulate there before saturating the pore central region. With the gas pressure increase, the adsorption peaks start to ease out. This is evidenced in Fig. 3b, where the relative difference between the adsorption peaks and the bulk densities is not as significant as that shown in Fig. 3a. At 29% and 50% of $CH_4$ (i. e., 71% and 50% of $CO_2$), the adsorption peaks of $CH_4$ near the kerogen surfaces disappear entirely. The ratio of $CO_2$ and $CH_4$ adsorption peak heights also become smaller as a result of the high pressure: 3.6 under the $CO_2$:$CH_4$ bulk molar ratio of ~3:1 and 1.4 under ~1:1. It is also worth noting from Fig. 3 that the adsorption layer is wider than one gas molecule size at the amorphous rough kerogen surfaces as indicated by the width of peaks in the density profiles.

In the 10 Å slit pore, the extreme nano-confinement leads to no distinction of the gas bulk region, with the two adsorption peaks at the upper and lower surfaces being collapsed into one as shown in Fig. 4 (also noticeable in Fig. 2). The pore boundaries are difficult to identify as the kerogen surfaces are amorphous and move upon adsorption. The adsorption region somewhat extends into the kerogen matrix and looks wider than 10 Å, which is the initial shortest distance between the two kerogen surfaces. Similarly, the adsorption density increases with the increase in the individual gas molar ratio under the constant total gas pressure. When the gas pressure is close to 30 MPa, the $CH_4$ adsorption is greatly enhanced, but this is not clearly seen for the $CO_2$ adsorption by comparing Fig. 4a and b. This indicates that the maximum $CO_2$ adsorption at the kerogen surfaces can be reached under a relatively small pressure. The slit pore gas adsorption amount is determined as the
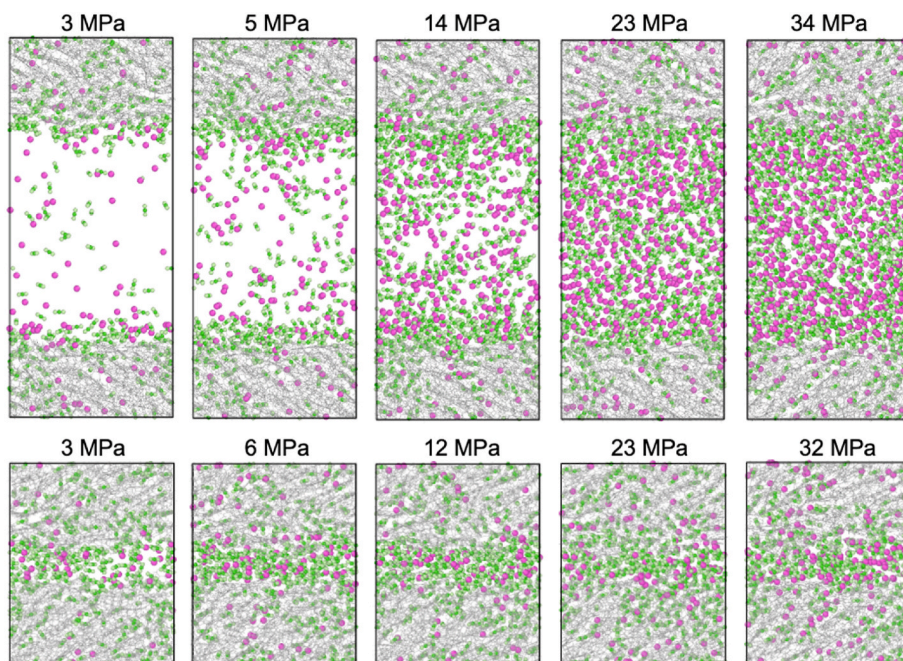
**Fig. 2.** Illustration of $CO_2$ (green) and $CH_4$ (plum) distributions in kerogen (grey) slit pores of 60 Å (first row) and 10 Å (second row) under varied pore pressures. The $CO_2$ bulk molar ratio in the mixture ranges from 50% to 55% (close to 1:1 $CO_2$–$CH_4$ mixture).
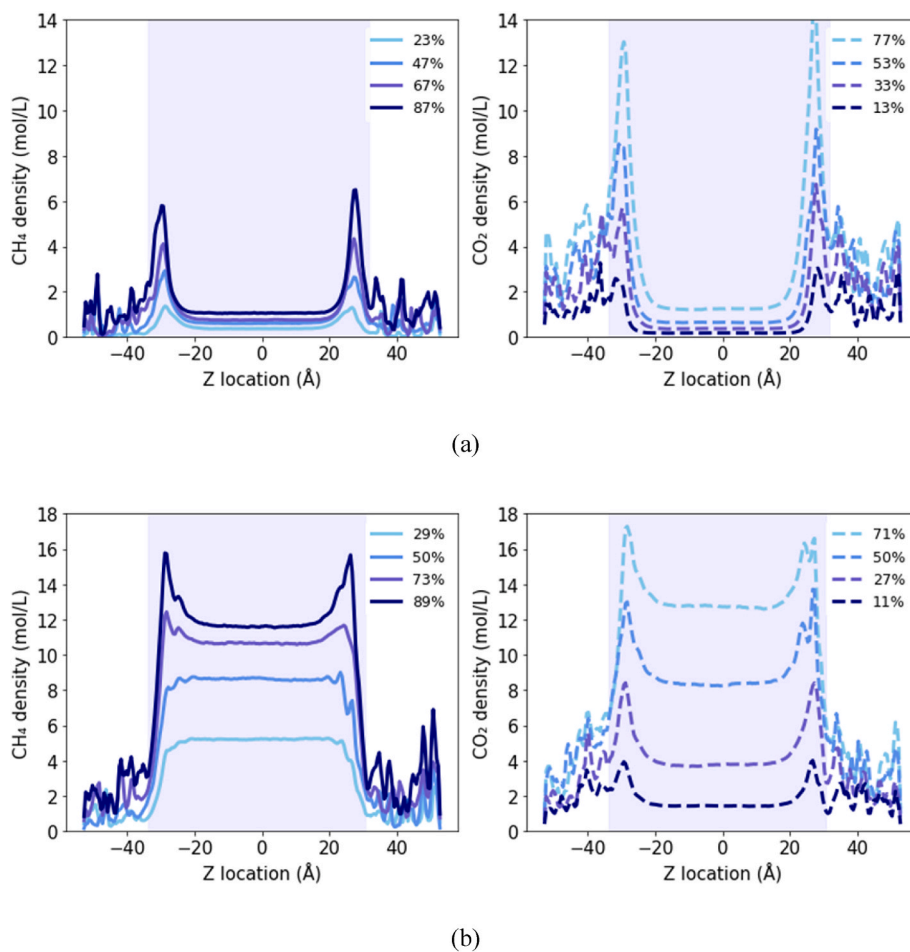


(a)



(b)

**Fig. 3.** $CH_4$ and $CO_2$ density distributions in the kerogen slit pore of 60 Å. Two typical pressure levels of (a) 3.0 ± 0.4 MPa and (b) 31.3 ± 1.6 MPa with the characteristic difference in density profiles are chosen. The gas compositions are signified by the varied colors according to their bulk molar ratios.
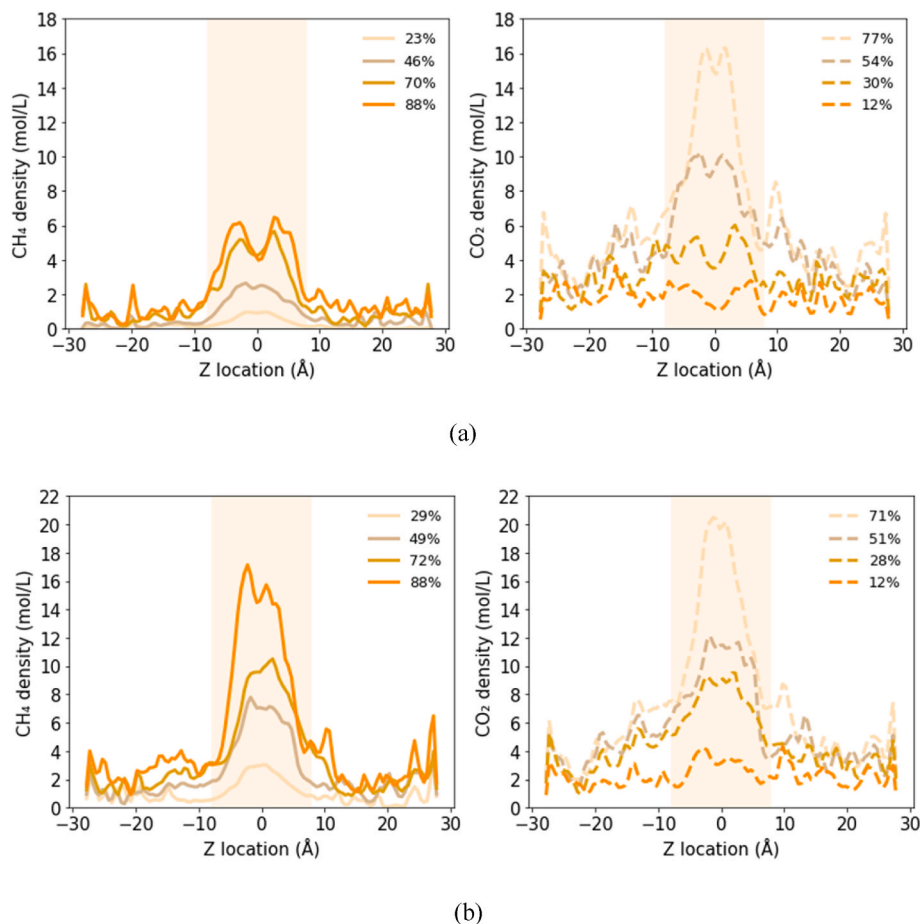
(a)



(b)

**Fig. 4.** CH$_4$ and CO$_2$ density distributions in the kerogen slit pore of 10 Å. Two typical pressure levels of (a) 2.6 ± 0.2 MPa and (b) 29.9 ± 1.0 MPa with the characteristic difference in density profiles are chosen. The gas composition is signified by varied colors according to bulk molar ratios.

sum of the free gas in the bulk and the adsorbed gas at the surfaces from the density profiles, shown as the shaded area in Figs. 3 and 4, and will be used for further discussions below.

### 3.2. Velocity profiles and relationship with CO$_2$ composition

The mass transport velocity profiles are calculated as the multiplication of density and velocity profiles for CO$_2$ and CH$_4$, respectively, and presented in Fig. 5. For easy comparison, they are normalized by the corresponding maximum mass velocity across the slit pore. A parabolic velocity profile is observed across the slit pore in all the simulated cases. The total mass flux throughout the matrix is marginal (the tiny peaks near zero at two sides of the parabola) compared to the slit pore, suggesting that large slit nanopores are the main pathways for gas transport. Therefore, we only focus on the gas transport in the slit pore in this study. There is observable fast mass transport near the kerogen surfaces at lower pressures as shown in Fig. 5a and b. This phenomenon is widely reported in the literature as surface diffusion [50–52]. As the gas pressure further increases to ~13 MPa and above, the diffusion-facilitated fast transport near kerogen surfaces becomes minimal and the mass transport is dominated by the viscous flow in the bulk gas region (Fig. 5c). Another interesting aspect to notice is that CH$_4$ surface diffusion is not as highlighted as CO$_2$ because of the preferential adsorption of CO$_2$ over CH$_4$ at kerogen surfaces, which suggests the possible selective mass transport between CO$_2$ and CH$_4$ with CO$_2$ having a large contribution from the surface adsorption to the total mass flux (the total mass flux is the integration of the mass transport velocity profile). The CO$_2$ and CH$_4$ mass transport profiles tend to be identical at high pressure. According to Fig. 5 overall, the CO$_2$–CH$_4$ composition does not

seem to have any noticeable impact on the normalized mass transport profiles.

The average gas mixture velocity (i.e., the volumetric flux divided by the initial pore size) under a unit pressure drop (i.e., normalized by the pressure drop) in the slit pores with size from 10 to 60 Å is plotted as a function of the CO$_2$ molar ratio in the bulk in Fig. 6. In general, the gas velocity drops fast with the pore size decrease ($V_{ave} \propto H^2$ in Hagen-Poiseuille flow, where $V_{ave}$ is the average gas velocity and $H$ is the pore size). CO$_2$ is a more viscous fluid than CH$_4$ at 300 K [53]. The addition of CO$_2$ increases the viscosity of the CO$_2$–CH$_4$ gas mixture, reducing the gas velocity under a given pressure by following a logarithmic decay (Fig. 6a, b and c). The fitted declining slope seems sharp at low pore pressures and gradually levels off at higher pressures. As the CO$_2$ molar ratio further increases in the bulk mixture, the average gas velocity tends to converge to a constant value, especially when the gas pressure is above 6 MPa. The main reason can be ascribed to the high CO$_2$ viscosity that constrains the gas mixture velocity within a low range after it transfers from the vapor to liquid phase (~6.7 MPa for pure phase [53]). The gas mixture velocity dependence on the CO$_2$ bulk molar ratio becomes weak in the slit pore of 10 Å as seen in Fig. 6d. As discussed in Section 3.1, the free gas region completely disappears in the pore center under the extreme confinement and the mass transport is dominated by the surface diffusion of the adsorbed phase. Therefore, the gas mixture velocity dependence on the CO$_2$ bulk ratio does not exactly follow the one in the 20–60 Å slit pores where the viscous flow is more pronounced (e.g., the case of 22.3 MPa). The noises are also likely related to the kerogen deformation since the adsorbed phase on the surfaces is affected more significantly by the kerogen surface morphology in the 10 Å slit pore. The average velocity in a single
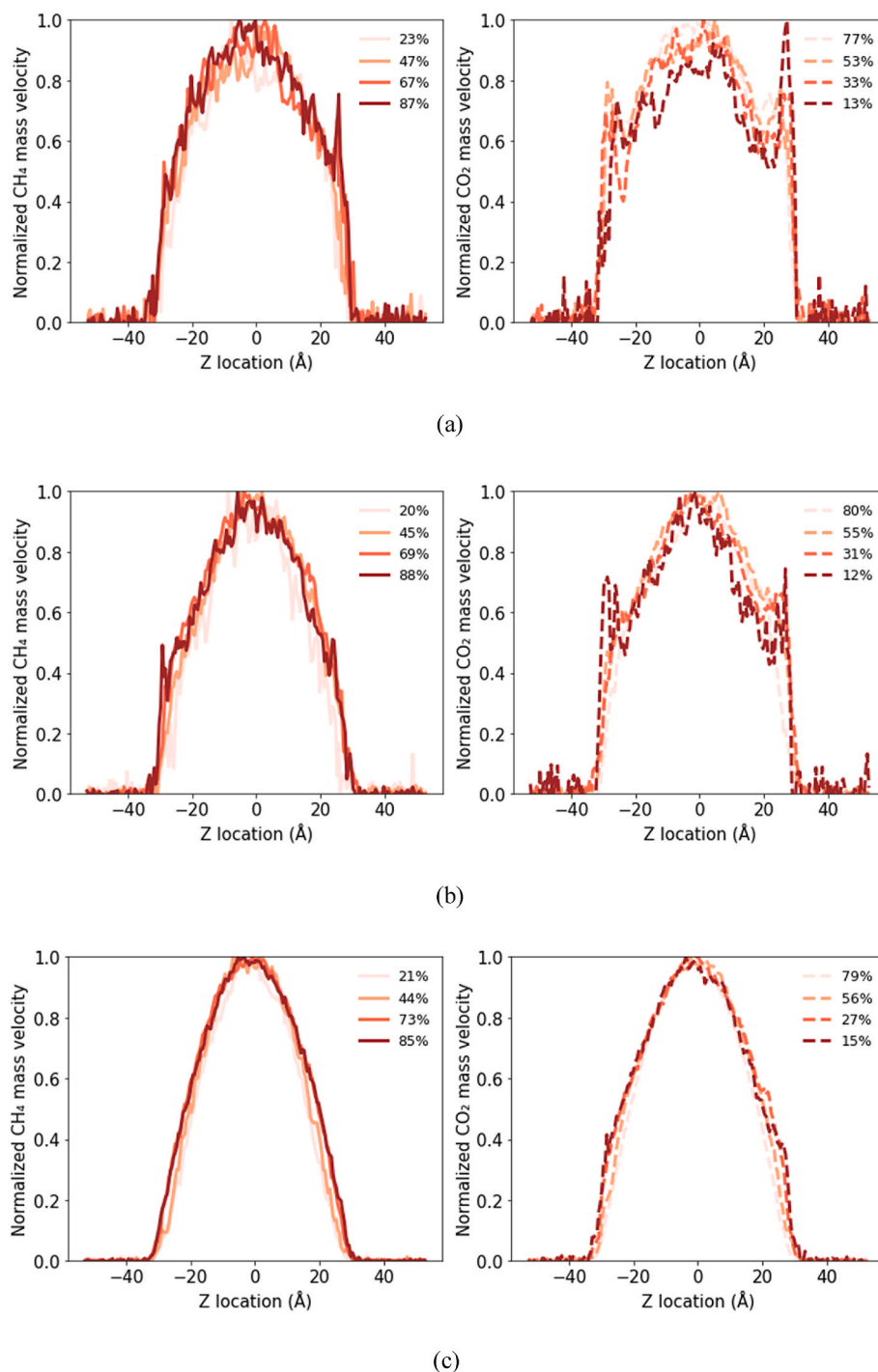
**Fig. 5.** Representative normalized CH$_4$ and CO$_2$ mass velocity profiles in the 60 Å kerogen slit pore under a pore pressure of (a) 3.0 ± 0.4 MPa, (b) 6.0 ± 0.7 MPa and (c) 12.8 ± 0.7 MPa. The varied colors show the change in CH$_4$ and CO$_2$ compositions in the bulk.

channel is usually calculated by the Hagen-Poiseuille equation ($V_{ave} = \frac{H^2 \nabla p}{12\mu}$, where $\mu$ is the viscosity). In the case of nano-confined CO$_2$–CH$_4$ mixtures, the viscosity greatly deviates from the bulk one due to the strong gas-gas and gas-solid interactions [33,54]. As it will be difficult to mathematically derive the velocity dependence on gas composition and pressure, future research may consider looking into the logarithmic decrease observed from our MD simulations.

After CO$_2$ is injected into the shale reservoir, it flows through the fracture network and diffuses into the organic matrix. Through competitive adsorption, CH$_4$ starts to desorb while CO$_2$ adsorbs. The gas mixture flowing towards the production well initially contains a large portion of CH$_4$, while CO$_2$ gradually increases its percentage in the gas mixture as CH$_4$ is depleted. It can be inferred that the overall gas production rate may decrease during the described process according to the dependence of gas velocity on the CO$_2$ ratio. In addition, the pressure sensitivity of the gas mixture velocity indicates that the CO$_2$ injection at a shallow geological depth under lower pressure may experience more fluctuation in recovery rate during the production process.

### 3.3. Adsorption selectivity
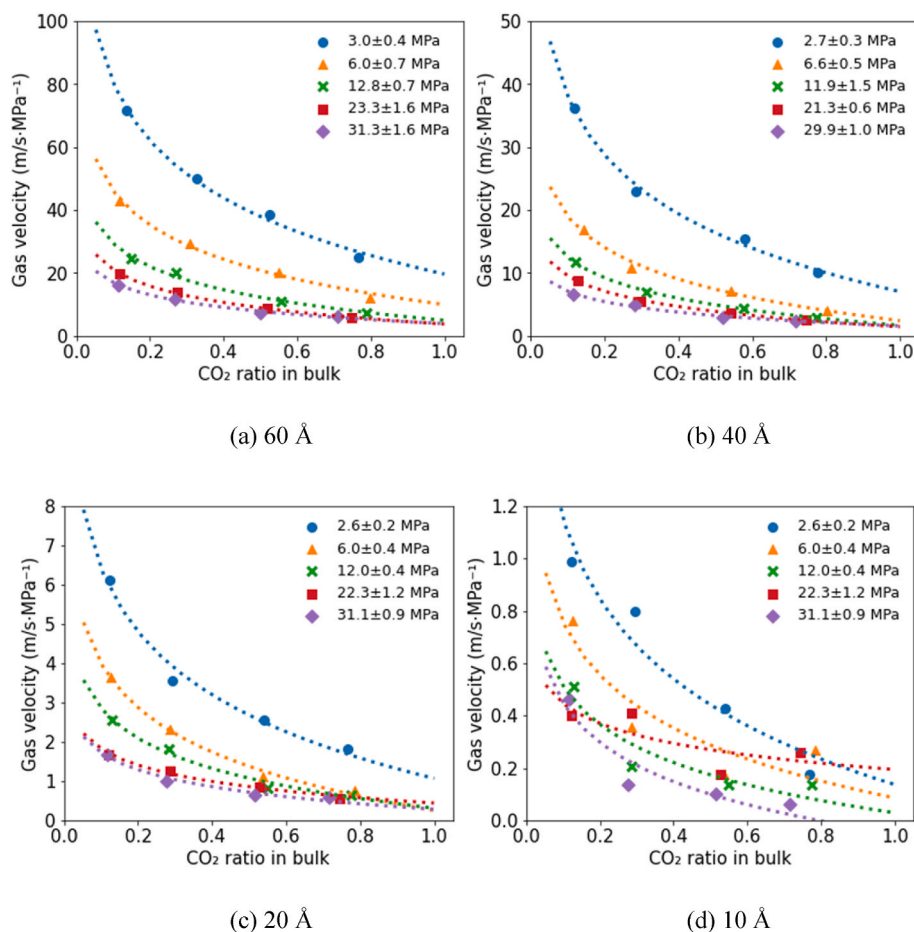
The competitive adsorption between CO$_2$ and CH$_4$ is commonly

Fig. 6. Normalized average $CO_2$–$CH_4$ gas mixture velocity as a function of the $CO_2$ molar ratio in the bulk phase across the kerogen slit pores of size (a) 60, (b) 40, (c) 20 and (d) 10 Å. The colored symbols indicate varied total pore gas pressures, and the dotted lines are showing logarithmic fittings of the data.

described by the adsorption selectivity

$$S_{ad} = \frac{n_{CO2}/n_{CH4}}{y_{CO2}/y_{CH4}} \qquad (2)$$

where, $n_{CO2}$ and $n_{CH4}$ are the absolute adsorption amounts of $CO_2$ and $CH_4$ in the slit pores, and $y_{CO2}$ and $y_{CH4}$ are the bulk molar ratios of $CO_2$ and $CH_4$. It can be seen from Fig. 7 that $CO_2$ is always preferentially adsorbed in the kerogen slit pore compared with $CH_4$ since the selectivity is greater than one in all the simulated cases. From 60 to 10 Å, the selectivity of $CO_2$ over $CH_4$ turns out to be more and more pronounced as the adsorbed density peaks at the lower and upper surfaces start to merge under the strong fluid-wall interactions: 1.1–2.0 in 60 Å (Fig. 7a), 1.2–2.4 in 40 Å (Fig. 7b), 1.5–2.9 in 20 Å (Fig. 7c) and 1.7–6.5 in 10 Å (Fig. 7d). The values generally agree well with experimental measurements. For example, the reported adsorption selectivities for organic-rich shale samples collected from the lower Silurian Longmaxi formation are 2.13–5.65 (323.15 K, <20 MPa) [10], 3.43–5.81 (303.15 K, 2–10 MPa) [9], and 3–8 (300–330 K, 1–11 MPa) [55]. The $CO_2$/$CH_4$ selectivity shows a linear-like decreasing trend [13,14] with the increase of the total gas pressure and the $CO_2$/$CH_4$ adsorption ratio approaches their ratio in the bulk phase (i.e., $CO_2$/$CH_4$ adsorption selectivity of ~1) at high pressures, possibly attributed to the smaller difference between the bulk gas density in the pore center and adsorption density at the surfaces (e.g., the contribution from the surface adsorption peaks to the slit pore adsorption becomes less significant). In comparison, the adsorption sites can be quickly taken over by $CO_2$ molecules at a low pore pressure. The accumulation of $CO_2$ near the kerogen surfaces in a great number causes a large density difference from the less-saturated

bulk, taking control of the total absolute gas adsorption amount in the slit pore. The adsorption selectivity seems not sensitive to the $CO_2$/$CH_4$ molar ratio. Theoretically, gas molecules will be adsorbed on the high-energy sites at low pressure, and the high-energy sites become gradually occupied as the pressure increases [56]. In the case of $CO_2$ and $CH_4$ mixtures, we understand that $CO_2$ may always quickly take over the high-energy sites at low pressure, and $CH_4$ only starts competing with $CO_2$ for low-energy sites at high pressure [14]. Since it is difficult for $CH_4$ to be adsorbed on the high-energy sites with $CO_2$ present, varying its ratio will not significantly affect the adsorption selectivity. In their experimental study, Qin et al. [57] also found that the $CO_2$/$CH_4$ adsorption selectivity varied slightly with the increasing $CH_4$ proportion in the mixed gas. The underlying mechanisms will be interesting for future investigations.

### 3.4. Mass transport selectivity

The selective mass transport of the $CO_2$–$CH_4$ mixture is analyzed as the mass transport selectivity

$$S_{mt} = \frac{f_{CO2}/f_{CH4}}{y_{CO2}/y_{CH4}} \qquad (3)$$

where, $f_{CO2}$ and $f_{CH4}$ are the molar mass fluxes of $CO_2$ and $CH_4$ in the slit pores. Fig. 8 presents the calculated mass transport selectivity as a function of gas pressure. It shows that the mass flux of $CO_2$ is generally higher than $CH_4$ regardless of their composition in the mixture and the slit pore size, with a maximum $S_{mt} = 7$ under ~3 MPa in the 10 Å slit pore. The $CO_2$/$CH_4$ mass flux selectivity follows a similar trend as their
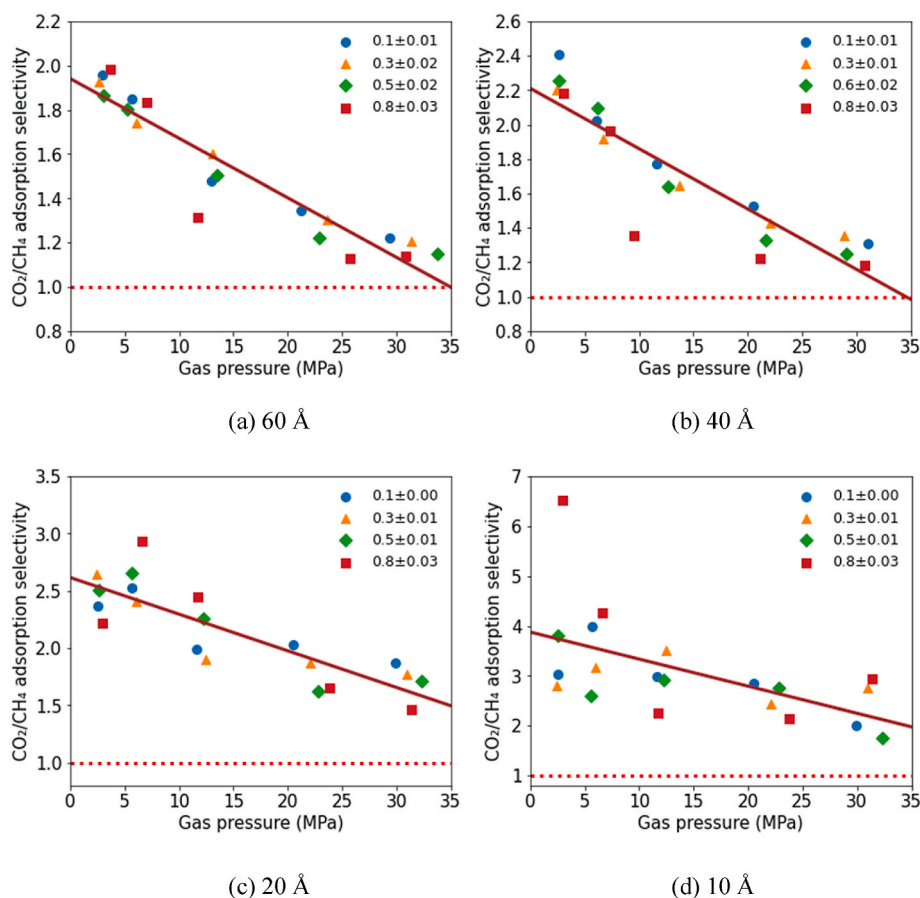
**Fig. 7.** $CO_2/CH_4$ adsorption selectivity as a function of pore gas pressure in the kerogen slit pores of size (a) 60, (b) 40, (c) 20 and (d) 10 Å. The colored symbols indicate varied $CO_2$ molar ratios in the bulk mixture.

adsorption selectivity with respect to the total gas pressure. This is because the mass flux is calculated from the integral of the mass velocity profile, and the preferential adsorption of $CO_2$ near the kerogen surfaces significantly contributes to the transport difference in masses. When the pore size decreases, the $CO_2/CH_4$ mass flux selectivity is also magnified, similar to the pattern of the adsorption selectivity. In large-scale continuum models, the $CO_2/CH_4$ transport selectivity is not commonly considered when simulating $CO_2$-EGR. However, the results here suggest that $CO_2$–$CH_4$ mixtures can show significant separation in the nanoporous organic matrix, which may affect the overall performance of the $CO_2$ injection and $CH_4$ production. Since gas transport within the organic matrix is often approximated as a diffusion process, a lumped $CO_2/CH_4$ transport selectivity can be potentially calculated for the organic matrix according to its nanopore size distribution and incorporated into the continuum-scale model as a ratio of the diffusion rates.

A summary of data with statistical analysis is provided in Fig. 9 to highlight the impact from several factors such as pore size, gas composition and surface diffusion on the mass transport selectivity. As can be seen from Fig. 9a, the $CO_2/CH_4$ mass flux selectivity goes down hyperbolically from 10 Å to 60 Å. In smaller nanopores, the $CO_2/CH_4$ mass flux selectivity spans over a much wider range (i.e., pressure-related variation). The variation of the mass flux selectivity eventually converges to a value close to unity as the pore size reaches 40 Å and above. In terms of the mixture composition, there is no strong evidence showing that the $CO_2/CH_4$ mass flux selectivity is correlated with the $CO_2$ molar ratio, as reported in Fig. 9b.

Coal has many similarities to kerogen as organic matter. Zhao et al. [58] have found that the transport diffusivity of $CO_2$ is always greater than that of $CH_4$ in coal matrix and the diffusion selectivity drops monotonically with the increasing pressure. In small pores, the diffusion

flux dominates over the viscous flux since there is no distinguishable bulk gas region so that the mass flux selectivity can reach very high. In large pores, the viscous flux would be more considerable than the diffusion flux. Viscous flow is driven by a pressure gradient and there is no selective transport when $CO_2$ and $CH_4$ are miscible gases flowing as a whole, and thus the mass flux selectivity would approach one. In order to evaluate the contribution of the surface diffusion to the selective gas transport, the $CO_2/CH_4$ mass flux in the bulk region (60 Å and 40 Å pores) is isolated for the selectivity calculation as shown in Fig. 9c. It can be seen that the $CO_2/CH_4$ mass flux selectivity becomes much closer to one after removing the contributions from the surface diffusion, suggesting the two individual components in the gas mixture flow at a similar rate in the bulk region of the slit pore. The effect of bulk diffusion can still be noticed when the pore gas pressure is smaller than 10 MPa, consistent with the findings in Zhao et al. [58].

## 4. Conclusions

In this study, we have systematically investigated the selective adsorption and transport of $CO_2$–$CH_4$ mixture with varied compositions in kerogen slit pores. It is revealed that both $CO_2/CH_4$ adsorption and transport selectivities are negatively correlated with the pore gas pressure and pore size, while not strongly affected by the $CO_2/CH_4$ bulk ratio. Although bulk diffusion can cause $CO_2/CH_4$ velocity separation, the selective mass transport of $CO_2$–$CH_4$ mixture is mostly resulted from the stronger surface diffusion of $CO_2$ that has a significant adsorbed amount at the kerogen surfaces. It is also worth noting that the average velocity of $CO_2$–$CH_4$ mixture in the kerogen slit pore decreases logarithmically with the increase of $CO_2$ molar ratio in the bulk phase. Such decrease becomes especially significant when the gas pressure is low in
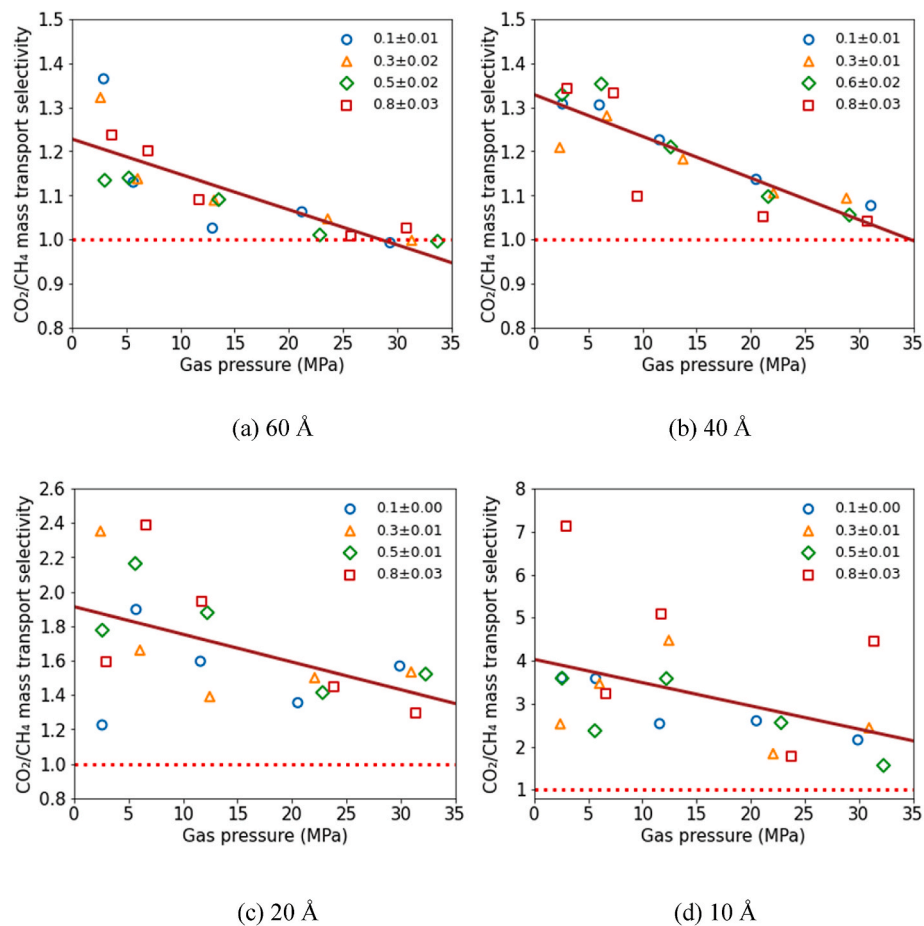
**Fig. 8.** $CO_2/CH_4$ mass transport selectivity as a function of pore gas pressure in the kerogen slit pores of size (a) 60, (b) 40, (c) 20 and (d) 10 Å. The colored symbols indicate the varied $CO_2$ molar ratios in the bulk mixture.
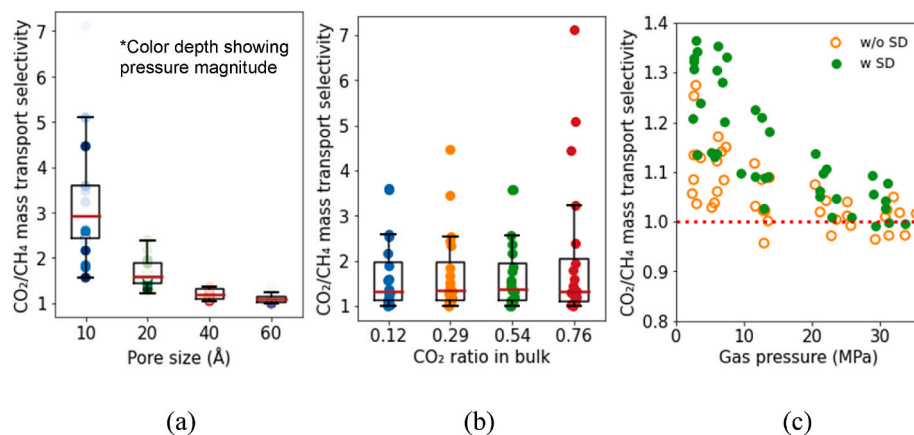


**Fig. 9.** $CO_2/CH_4$ mass transport selectivity as a function of (a) pore size and (b) $CO_2$ molar ratio in the bulk mixture. (c) $CO_2/CH_4$ mass transport selectivity in the entire slit pore with surface diffusion (w SD) and bulk gas region without surface diffusion (w/o SD) (only showing the data in the 60 and 40 Å slit pores).

large pores. These new results indicate that the selective mass transport of $CO_2$–$CH_4$ in low-porosity shale reservoirs is important and should not be neglected in the large-scale simulations of $CO_2$-EGR.

**Credit author statement**

Jian Wu: Conceptualization, Methodology, Investigation, Validation, Visualization, Writing – original draft, Luming Shen: Conceptualization, Writing – review & editing, Supervision, Funding acquisition, Pengyu

Huang: Methodology, Investigation, Writing – review & editing, Yixiang Gan: Investigation, Writing – review & editing, Supervision.

**Declaration of competing interest**

The authors declare that they have no known competing financial interests or personal relationships that could have appeared to influence the work reported in this paper.

## Data availability

Data will be made available on request.

## Acknowledgments

## Appendix A. Supplementary data

Supplementary data to this article can be found online at https://doi.org/10.1016/j.energy.2023.127224.

## References

[1] Zendehboudi S, Bahadori A. Shale oil and gas handbook: theory, technologies, and challenges. Gulf Professional Publishing; 2016.

[2] Singh U. Carbon capture and storage: an effective way to mitigate global warming. Curr Sci 2013;105(7):914–22.

[3] GHD. New global carbon capture, utilisation and storage team leads on world's largest project. https://www.ghd.com/en/news/new-global-carbon-capture-utilisation-and-storage-team-leads-on-world-s-largest-project.aspx;; 2022.

[4] Zoback MD, Gorelick SM. Earthquake triggering and large-scale geologic storage of carbon dioxide. Proc Natl Acad Sci U S A 2012;109(26):10164–8.

[5] Neil CW, Mehana M, Hjelm RP, Hawley ME, Watkins EB, Mao Y, et al. Reduced methane recovery at high pressure due to methane trapping in shale nanopores. Commun Earth Environ 2020;1(1).

[6] Louk K, Ripepi N, Luxbacher K, Gilliland E, Tang X, Keles C, et al. Monitoring CO2 storage and enhanced gas recovery in unconventional shale reservoirs: results from the Morgan County, Tennessee injection test. J Nat Gas Sci Eng 2017;45:11–25.

[7] Liu F, Ellett K, Xiao Y, Rupp JA. Assessing the feasibility of CO2 storage in the New Albany Shale (Devonian–Mississippian) with potential enhanced gas recovery using reservoir simulation. Int J Greenh Gas Control 2013;17:111–26.

[8] Liu J, Yao Y, Liu D, Elsworth D. Experimental evaluation of CO 2 enhanced recovery of adsorbed-gas from shale. Int J Coal Geol 2017;179:211–8.

[9] Liu J, Xie L, Elsworth D, Gan Q. CO2/CH4 competitive adsorption in shale: implications for enhancement in gas production and reduction in carbon emissions. Environ Sci Technol 2019;53(15):9328–36.

[10] Xie W, Wang M, Chen S, Vandeginste V, Yu Z, Wang H. Effects of gas components, reservoir property and pore structure of shale gas reservoir on the competitive adsorption behavior of CO2 and CH4. Energy 2022:254.

[11] Qin C, Jiang Y, Zuo S, Chen S, Xiao S, Liu Z. Investigation of adsorption kinetics of CH4 and CO2 on shale exposure to supercritical CO2. Energy 2021:236.

[12] Sun J, Chen C, Zhang Y, Li W, Song Y. Competitive adsorption characteristics based on partial pressure and adsorption mechanism of CO2/CH4 mixture in shale pores. Chem Eng J 2022:430.

[13] Ho TA, Wang Y, Xiong Y, Criscenti LJ. Differential retention and release of CO2 and CH4 in kerogen nanopores: implications for gas extraction and carbon sequestration. Fuel 2018;220:1–7.

[14] Huang L, Ning Z, Wang Q, Zhang W, Cheng Z, Wu X, et al. Effect of organic type and moisture on CO2/CH4 competitive adsorption in kerogen with implications for CO2 sequestration and enhanced CH4 recovery. Appl Energy 2018;210:28–43.

[15] Sui H, Zhang F, Wang Z, Wang D, Wang Y. Effect of kerogen maturity, water content for carbon dioxide, methane, and their mixture adsorption and diffusion in kerogen: a computational investigation. Langmuir 2020;36(33):9756–69.

[16] Wang T, Tian S, Li G, Sheng M, Ren W, Liu Q, et al. Molecular simulation of CO2/CH4 competitive adsorption on shale kerogen for CO2 sequestration and enhanced gas recovery. J Phys Chem C 2018;122(30):17009–18.

[17] Li J, Sun C. Molecular insights on competitive adsorption and enhanced displacement effects of CO2/CH4 in coal for low-carbon energy technologies. Energy 2022:261.

[18] Yang X, Chen Z, Liu X, Xue Z, Yue F, Wen J, et al. Correction of gas adsorption capacity in quartz nanoslit and its application in recovering shale gas resources by CO2 injection: a molecular simulation. Energy 2022:240.

[19] Klewiah I, Berawala DS, Alexander Walker HC, Andersen PØ, Nadeau PH. Review of experimental sorption studies of CO2 and CH4 in shales. J Nat Gas Sci Eng 2020; 73.

[20] Kang D, Wang X, Zheng X, Zhao Y-P. Predicting the components and types of kerogen in shale by combining machine learning with NMR spectra. Fuel 2021: 290.

[21] Sun H, Zhao H, Qin N, Li Y. Molecular insights into the enhanced shale gas recovery by carbon dioxide in kerogen slit nanopores. J Phys Chem C 2017;121(18): 10233–41.

[22] Ho TA, Wang Y. Molecular origin of wettability alteration of subsurface porous media upon gas pressure variations. ACS Appl Mater Interfaces 2021;13(34): 41330–8.

[23] Liu K, Ostadhassan M, Zhou J, Gentzis T, Rezaee R. Nanoscale pore structure characterization of the Bakken shale in the USA. Fuel 2017;209:567–78.

[24] Gou Q, Xu S, Hao F, Yang F, Shu Z, Liu R. The effect of tectonic deformation and preservation condition on the shale pore structure using adsorption-based textural quantification and 3D image observation. Energy 2021:219.

[25] Javadpour F, Fisher D, Unsworth M. Nanoscale gas flow in shale gas sediments. J Can Petrol Technol 2007;46(10).

[26] Javadpour F, Singh H, Rabbani A, Babaei M, Enayati S. Gas flow models of shale: a review. Energy Fuel 2021;35(4):2999–3010.

[27] Sun Z, Li X, Liu W, Zhang T, He M, Nasrabadi H. Molecular dynamics of methane flow behavior through realistic organic nanopores under geologic shale condition: pore size and kerogen types. Chem Eng J 2020:398.

[28] Wang Y, Aryana SA. Coupled confined phase behavior and transport of methane in slit nanopores. Chem Eng J 2021:404.

[29] Hu Y, Liu G, Luo N, Gao F, Yue F, Gao T. Multi-field coupling deformation of rock and multi-scale flow of gas in shale gas extraction. Energy 2022:238:121666.

[30] Yang X, Zhou W, Liu X, Yan Y. A multiscale approach for simulation of shale gas transport in organic nanopores. Energy 2020:210.

[31] Liu B, Qi C, Mai T, Zhang J, Zhan K, Zhang Z, et al. Competitive adsorption and diffusion of CH4/CO2 binary mixture within shale organic nanochannels. J Nat Gas Sci Eng 2018;53:329–36.

[32] Kazemi M, Takbiri-Borujeni A. Selective adsorption and transport diffusion of CO2-CH4 binary mixture in carbon-based organic nanopores. SPE Western Regional Meeting. OnePetro; 2017.

[33] Firouzi M, Wilcox J. Slippage and viscosity predictions in carbon micropores and their influence on CO2 and CH4 transport. J Chem Phys 2013;138(6):064705.

[34] Wu T, Firoozabadi A. Molecular simulations of binary gas mixture transport and separation in slit nanopores. J Phys Chem C 2018;122(36):20727–35.

[35] Ho TA, Wang Y. Pore size effect on selective gas transport in shale nanopores. J Nat Gas Sci Eng 2020;83.

[36] Liu L, Nieto-Draghi C, Lachet V, Heidaryan E, Aryana SA. Bridging confined phase behavior of CH4-CO2 binary systems across scales. J Supercrit Fluids 2022:189.

[37] Ungerer P, Collell J, Yiannourakou M. Molecular modeling of the volumetric and thermodynamic properties of kerogen: influence of organic type and maturity. Energy Fuel 2014;29(1):91–105.

[38] Wu J, Huang P, Maggi F, Shen L. Effect of sorption-induced deformation on methane flow in kerogen slit pores. Fuel 2022;325:124886.

[39] Wang J, Wolf RM, Caldwell JW, Kollman PA, Case DA. Development and testing of a general amber force field. J Comput Chem 2004;25(9):1157–74.

[40] Huang P, Shen L, Maggi F, Chen Z, Pan Z. Influence of surface roughness on methane flow in shale kerogen nano-slits. J Nat Gas Sci Eng 2022:104650.

[41] Potoff JJ, Siepmann JI. Vapor–liquid equilibria of mixtures containing alkanes, carbon dioxide, and nitrogen. AIChE J 2001;47(7):1676–82.

[42] Eggimann BL, Sun Y, DeJaco RF, Singh R, Ahsan M, Josephson TR, et al. Assessing the quality of molecular simulations for vapor–liquid equilibria: an analysis of the TraPPE database. J Chem Eng Data 2019;65(3):1330–44.

[43] Martin MG, Siepmann JI. Transferable potentials for phase equilibria. 1. United-atom description of n-alkanes. J Phys Chem B 1998;102(14):2569–77.

[44] Hockney RW, Eastwood JW. Computer simulation using particles. crc Press; 1988.

[45] Wu J, Huang P, Maggi F, Shen L. Molecular investigation on CO2-CH4 displacement and kerogen deformation in enhanced shale gas recovery. Fuel 2022;315:123208.

[46] Peng D-Y, Robinson DB. A new two-constant equation of state. Ind Eng Chem Fundam 1976;15(1):59–64.

[47] Li Z, Jun Y, Kou J. Mixture composition effect on hydrocarbon-water transport in shale organic nanochannels. J Phys Chem Lett 2019;10(15):4291–6.

[48] Thompson AP, Aktulga HM, Berger R, Bolintineanu DS, Brown WM, Crozier PS, et al. LAMMPS-A flexible simulation tool for particle-based materials modeling at the atomic, meso, and continuum scales. Comput Phys Commun 2021:108171.

[49] Stukowski A. Visualization and analysis of atomistic simulation data with OVITO–the Open Visualization Tool. Model Simulat Mater Sci Eng 2009;18(1): 015012.

[50] Liu L, Wang Y, Aryana SA. Insights into scale translation of methane transport in nanopores. J Nat Gas Sci Eng 2021:96.

[51] Yu H, Fan J, Chen J, Zhu Y, Wu H. Pressure-dependent transport characteristic of methane gas in slit nanopores. Int J Heat Mass Tran 2018;123:657–67.

[52] Zhao Y, Luo M, Liu L, Wu J, Chen M, Zhang L. Molecular dynamics simulations of shale gas transport in rough nanopores. J Petrol Sci Eng 2022:217.

[53] Linstrom P, Mallard W. NIST chemistry WebBook, NIST standard reference database number 69. Gaithersburg MD: National Institute of Standards and Technology; 2022, 20899.

[54] Wang S, Javadpour F, Feng Q. Fast mass transport of oil and supercritical carbon dioxide through organic nanopores in shale. Fuel 2016;181:741–58.

[55] Lu T, Zeng K, Jiang P, Zhou B, Xu R. Competitive adsorption in CO2 enhancing shale gas: low-field NMR measurement combined with molecular simulation for selectivity and displacement efficiency model. Chem Eng J 2022:440.

[56] Li J, Wu K, Chen Z, Wang W, Yang B, Wang K, et al. Effects of energetic heterogeneity on gas adsorption and gas storage in geologic shale systems. Appl Energy 2019;251:113368.

[57] Qin C, Jiang Y, Zhou J, Song X, Liu Z, Li D, et al. Effect of supercritical CO2 extraction on CO2/CH4 competitive adsorption in Yanchang shale. Chem Eng J 2021:412.

[58] Zhao Y, Feng Y, Zhang X. Selective adsorption and selective transport diffusion of CO2-CH4 binary mixture in coal ultramicropores. Environ Sci Technol 2016;50 (17):9380–9.